The Impact of Altimeter Sampling Patterns on Estimates of Background Errors in a Global Wave Model

DIANA J. M. GREENSLADE

Bureau of Meteorology Research Centre, Bureau of Meteorology, Melbourne, Australia

IAN R. YOUNG

Swinburne University of Technology, Melbourne, Australia

(Manuscript received 19 March 2004, in final form 10 January 2005)

ABSTRACT

One of the main limitations to current wave data assimilation systems is the lack of an accurate representation of the structure of the background errors. One method that may be used to determine background errors is the observational method of Hollingsworth and Lönnberg. The observational method considers correlations of the differences between observations and the background. For the case of significant wave height (SWH), potential observations come from satellite altimeters. In this work, the effect of the irregular sampling pattern of the satellite on estimates of background errors is examined. This is achieved by using anomalies from a 3-month mean as a proxy for model errors. A set of anomaly correlations is constructed from modeled wave fields. The isotropic length scales of the anomaly correlations are found to vary considerably over the globe. In addition, the anomaly correlations are found to be significantly anisotropic. The modeled wave fields are then sampled at simulated altimeter observation locations, and the anomaly correlations are recalculated from the simulated altimeter data. The results are compared to the original anomaly correlations. It is found that, in general, the simulated altimeter data can capture most of the geographic and seasonal variability in the isotropic anomaly correlation length scale. The best estimates of the isotropic length scales come from a method in which correlations are calculated between pairs of observations from prior and subsequent ground tracks, in addition to along-track pairs of observations. This method was found to underestimate the isotropic anomaly correlation length scale by approximately 10%. The simulated altimeter data were not so successful in producing realistic anisotropic correlation functions. This is because of the lack of information in the zonal direction in the simulated altimeter data. However, examination of correlations along ascending and descending ground tracks separately can provide some indication of the areas on the globe for which the anomaly correlations are more anisotropic than others.

1. Introduction

Several forecasting centers around the world run operational wave forecasting models that routinely assimilate satellite significant wave height (SWH) data or, more recently, directional wave spectra. There has been a considerable amount of research into the development of wave data assimilation systems in recent years. A significant limitation to current assimilation systems is the specification of the model (or background) errors. This has not previously been explored to any great extent for wave models.

One method commonly used to investigate the background errors is the observational method of Hollingsworth and Lönnberg (1986). The observational method considers correlations of the differences between observations and the background. For the case of SWH, potential observations come from satellite altimeters. The main aim of this paper is to determine the feasibility of using satellite altimeters to determine background errors. In particular, it is important to know if the irregular sampling pattern of the satellite has any effect on the results. It is this issue that is addressed in this work.

The approach taken is to use model anomaly corre-

Corresponding author address: Dr. Diana J. M. Greenslade, Bureau of Meteorology Research Centre, GPO Box 1289K, Melbourne VIC 3001, Australia.
E-mail: dag@bom.gov.au

lations as a proxy for background error correlations. A set of model anomaly correlations is constructed from global modeled wave fields. The modeled wave fields are then sampled along simulated satellite altimeter ground tracks, and the anomaly correlations are recalculated from this simulated altimeter data. These are compared to the full model anomaly correlations to determine the impact of the irregular sampling pattern of the satellite altimeter.

A brief review of previous wave data assimilation research is given in section 2 with an emphasis on specification of the wave model background errors. In section 3, the modeled wave fields used in this work are described. Section 4 presents the anomaly correlations from the modeled wave fields, and section 5 presents the anomaly correlations from the simulated altimeter observations. Further analysis of the results is described in section 6, and, finally, a summary and outlook are presented.

2. Background

Current operational wave data assimilation systems at, for example, the European Centre for Medium-Range Weather Forecasts (ECMWF), the Australian Bureau of Meteorology (the Bureau) and Météo-France use the sequential method of statistical interpolation (SI) (Lorenc 1981) to combine first-guess (or background) wave model fields with the observations to obtain analyzed wave fields. Details of the SI algorithm can be found in Lionello et al. (1992) or Greenslade (2001). One of the major limitations in the application of SI techniques is the specification of the background error correlation matrix **P**. This is a symmetric $N_{\text{obs}} \times N_{\text{obs}}$ matrix (N_{obs} is the number of observations) whose element (k, j) is given by

$$P_{kj} = \frac{\langle (H_p^k - T^k)(H_p^j - T^j) \rangle}{\sigma_p^k \sigma_p^j}, \tag{1}$$

where H_p is the model first guess, T is the true field, $\langle\rangle$ is the expected value, and σ_p is the model prediction root-mean-square (rms) error; that is,

$$\sigma_p^i = \sqrt{\langle (H_p^i - T^i)^2 \rangle}. \tag{2}$$

In other words, the value of element (k, j) of matrix **P** is the correlation between the background error at observation location k and the background error at observation location j.

A wide range of structures has been used in the literature to describe **P**. A full description of these can be found in Greenslade (2004). They generally have the form

TABLE 1. Values of the parameters in Eq. (3) used by various authors.

Author	a	b	c	L
Lionello et al. (1992)	0	1	1	15°
Mastenbroek et al. (1994)	1	1	1	~135 km
Breivik and Reistad (1994)	0	2	½	200–40 km
Young and Glowacki (1996)	0	2	½	350 km
Greenslade (2001)	0	2	½	300 km
Voorrips et al. (1997)	0	3/2	1	200 km

$$P_{kj} = \left(1 + \frac{|\mathbf{x}_k - \mathbf{x}_j|}{L}\right)^a \exp\left[-c\left(\frac{|\mathbf{x}_k - \mathbf{x}_j|}{L}\right)^b\right], \tag{3}$$

where L is the decorrelation length scale and $|\mathbf{x}_k - \mathbf{x}_j|$ is the distance between the points k and j. The values of a, b, c, and L used by various authors are listed in Table 1 and some of the resulting P_{kj} curves are plotted in Fig. 1.

Some of these structures for P_{kj} have been ad hoc estimates, while others have provided some justification for the choice of background error structure. All of the studies have assumed isotropy and homogeneity in the background error structure, with the exception of the studies in which L is defined in degrees. (This results in a larger zonal spatial scale at lower latitudes than at high latitudes.) To date, there has been no extensive effort made to determine the spatial scale of the background errors in wave models on a global basis. A major limitation to current implementations of SI systems, and, indeed, potential future systems, is the lack of an accurate representation of the background errors.

The background error is, by definition, the difference between the background and the truth. Of course, the truth is not known, and so other methods to calculate background error must be sought. There are several

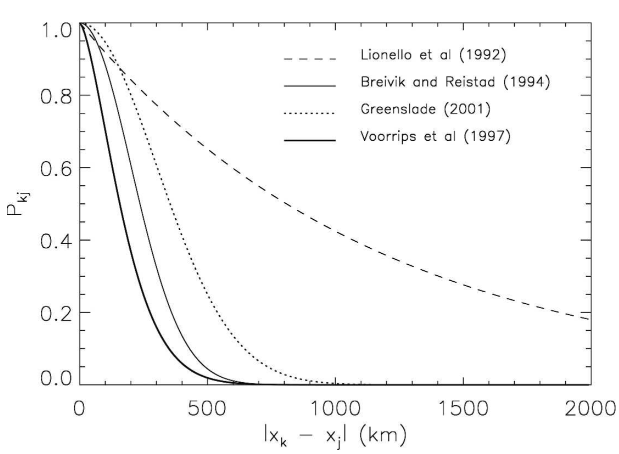

FIG. 1. Some example functions used for the background error correlations at midlatitudes.

methods that have commonly been used to estimate the background error correlations in meteorology and oceanography. One of these is the observational method of Hollingsworth and Lönnberg (1986).

The observational method has the merit of being a technique that calculates background errors directly. It can be used to determine both the background error variance and its spatial structure. This method considers observations from a long-term, dense, homogenous observational network and examines the difference between the observations and the background field. Highest-quality wave observations generally come from buoys or platforms that are fixed in space. However, the spatial distribution of buoys is extremely poor, for practical reasons they are generally located in coastal regions, and so it is difficult to obtain any information on the spatial error correlation structure from buoy data. This lack of a long-term observational network with reasonable space–time sampling characteristics over the ocean means that it has been difficult in the past to apply the observational method within the fields of oceanography or marine meteorology.

However, satellite altimeters now provide a comprehensive global long-term network of wave observations that could potentially be used to determine the correlation structure of the background errors in a wave model. Before doing so, it is necessary to determine what effect, if any, the irregular sampling pattern of the satellite has on the error calculations.

3. Wave model

The wave model used in this work is the Australian Bureau of Meteorology Wave Model (AUSWAM; National Meteorological Operations Centre 1999), a version of the Wave Model (WAM). WAM (The WAMDI Group 1988; Komen et al. 1994) is a third-generation wave model that solves the wave transport equation explicitly without assuming a form for the evolving spectrum. AUSWAM incorporates the physics of Snyder et al. (1981) with increased dissipation and third-order upwinding numerics (Bender 1996).

Wave spectra are discretized into 12 directional bins, centered at 15°, 45°, 75°, etc. This "staggering" of the directional bins is to avoid having spectral energy propagating directly along the axes of the north–south coordinate system (Bidlot et al. 1997). There are 25 frequency bins ranging from 0.0418 to 0.4114 Hz. Deep water physics only is used. The propagation and source-term time steps are 20 and 10 min, respectively. For the global version of the model, the north–south extent of the domain is 78°N–78°S.

Forcing fields for the global wave model are wind velocities at 10 m above sea level. These are obtained from the Bureau's global atmospheric model, GASP (Seaman et al. 1995). Surface winds are obtained from the lowest level of GASP via Monin–Obukhov theory with empirical stability functions (Garratt 1992). The 10-m wind fields are instantaneous "snapshots" of the surface and are provided to the wave model at 12-hourly intervals and 2.5° spatial resolution. These are linearly interpolated in time to 3-hourly intervals, and bilinearly interpolated in space to the resolution of the wave model grid. Two 3-month periods are examined in this work: July–September 1998 and January–March 1999. On 9 December 1998, there was a major upgrade to GASP (National Meteorological Operations Centre 1998) in which the spatial resolution was increased from T79 to T239. However, the spatial resolution of the surface winds used to force the wave model was not altered at this time.

For the modeled wave fields used in this work, the wave model was implemented at 0.5° spatial resolution globally. Only wave model hindcasts are used here. These are modeled wave fields that have been forced by surface winds obtained from the data assimilation cycle of the atmospheric model. No wave data assimilation is used in the construction of the modeled wave fields. Fields of integrated wave parameters (in particular, SWH) are used every 6 h.

4. Anomaly correlations from wave model

The background error correlation matrix in Eq. (1) can be expressed as the spatial error correlation between two points, j and k, that is (Daley 1991),

$$R_{jk} = \frac{\overline{(O_j - B_j)(O_k - B_k)}}{\sqrt{\overline{(O_j - B_j)^2}\,\overline{(O_k - B_k)^2}}} = \rho(r, \theta), \qquad (4)$$

where ρ is the error correlation as a function of great circle distance r and angle θ, the overbar represents a time average, O_i are "observations," and B_i represent the background values.

a. Correlation computations

Details of how the spatial correlation function [R_{jk} in Eq. (4)] is calculated are presented here. The time period and domain over which R_{jk} is calculated first needs to be specified. A range of domains and time periods was initially examined. Time periods that were considered ranged from 1 to 12 months, and the spatial domains considered were boxes with side lengths of 10°, 20°, and 30° in latitude and longitude. The size of the domain can play an important role, because fields of SWH are typically not homogenous over the ocean. Generally, the larger the area considered, the larger the length scale of the correlation. This is discussed in more detail in section 6c. On the other hand, on time scales of weeks to months, SWH can be assumed to be stationary, so the time period chosen has less of an impact on the correlation functions than the box size. The selected time periods and box sizes were partly dictated by the altimeter sampling pattern.

The time period chosen needed to be long enough so that at any location, there were several repeat observations from the altimeter. It was also desirable to have it short enough to enable detection of any seasonality in the correlations. Thus, a time period of 3 months was chosen. The spatial dimensions of the box needed to be large enough so that prior and subsequent altimeter ground tracks could be used (this is discussed in detail in section 5a). However, the motivation for this work is data assimilation; in data assimilation processes, one is most interested in what happens at small spatial scales. A box with side lengths of 20° in latitude and 20° in longitude was found to be the best compromise between these two requirements. For the remainder of this section, the "domain" refers to a 20° box in latitude and longitude, unless otherwise specified.

For each pair of grid points j, k within the domain, R_{jk} was calculated according to Eq. (4). Background errors are simulated by using the 3-month model mean as the background field and using the individual 6-hourly modeled wave fields within that time period to represent realizations of that field. Therefore, in Eq. (4), O_i are the 6-hourly modeled SWH values and B_i are values of the 3-month model mean, that is,

$$B_i = \overline{O_i} = \frac{1}{N_t}\sum_{t=1}^{N_t} O_i(t), \tag{5}$$

where N_t is the number of 6-hourly model fields within the 3-month time period. In addition, the great circle distance r (km) and θ the great circle bearing (angle in degrees clockwise from north) between points j and k are calculated. It can be seen that the "background errors" considered here are, in fact, anomalies from a 3-month climatological average. So the simulated background error correlations considered in this section are actually anomaly correlations, and will be referred to as such for the remainder of this work. The "model climatology" will refer to the 3-month mean model field.

The anomaly correlation functions $\rho(r, \theta)$ were averaged into bins of 1-km radius and 1° angle. Figure 2a shows an example of the anomaly correlation for a 20° box centered at 0°N, 60°E, that is, on the equator in the

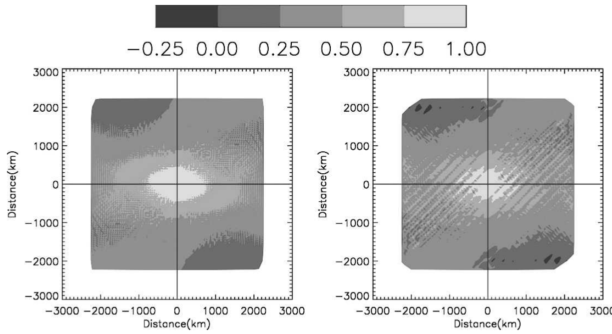

FIG. 2. Model error correlations for a box of size 20° × 20° centered at 0°, 60°E for the 3-month time period 1 Jul–30 Sep 1998 (a) using all model grid points and (b) using every fifth model grid point.

Indian Ocean for the 3-month time period of 1 July–30 September 1998. Note that, by definition, $R_{jk} = R_{kj}$, and so the function is invariant under a 180° rotation.

As expected, the correlations are highest at short distances and decay toward longer distances. This behavior can be interpreted as follows. Consider a model grid point within the domain. Assume that at this grid point, at a particular time, the deviation in SWH from the model climatology is large. Then, first, and most obviously, it can be seen that the SWH at points close to this grid point is also likely to deviate strongly from the climatology, whereas SWH at points further away is less likely to deviate strongly from the climatology.

For this particular region, the decay in the correlation function is slower in the zonal direction than the meridional direction; that is, correlations are larger in the east–west direction than the north–south direction. From this elongated shape of the correlation function, it can, therefore, be seen that a grid point x km to the east or west is more likely to have a large deviation from the climatology than a point x km to the north or south. Similarly, if SWH at this grid point is close to the climatology, then points to the east or west are more likely to be close to the climatological values than points to the north or south. If the climatology were constant over the domain, then this correlation function would indicate that during this time period, the dominant features of the SWH field are elongated in the east–west direction. There is no information on the direction in which these features are propagating because all of the calculations are carried out on instantaneous fields; that is, there is no time-dependent information in the correlations. However, with the added knowledge that the surface winds in this region during this time are predominantly westerlies (Piexoto and Oort 1992), it can be inferred that the behavior described above is likely to be a result of wave systems in this domain, propagating predominantly in the zonal direction.

While not essential for this study, to reduce computational time the model grid was subsampled for the correlation calculations. The equivalent correlation with only every fifth model grid point used in the calculations is shown in Fig. 2b. It can be seen that although the resolution here is coarser, and there is a "banded" effect in the correlation function, the major features of this plot are similar to those in Fig. 2a. For the remainder of this work, all anomaly correlations presented are those using every fifth model grid point.

b. *Fitting to analytic functions*

The aim of this work is to determine the impact of the irregular altimeter sampling pattern on estimates of error correlations. To enable a quantitative assessment of this, an analytic description of the anomaly correlation is required. The calculated anomaly correlations $\rho(r, \theta)$ were, therefore, fitted to analytic functions. A commonly used function in studies of surface pressure and temperature error correlations (Julian and Thiebaux 1975; Seaman 1982) is

$$\rho(r, \theta) = [a_4 \cos(a_5 d) + a_6 - a_4] \exp\left[-\frac{d}{a_3}\right], \tag{6}$$

where

$$d^2 = r^2\left(\frac{1}{a_1^2}\cos^2(\theta - a_2) + a_1^2 \sin^2(\theta - a_2)\right). \tag{7}$$

The justification for including a cosine dependency in Eq. (6) is that often the temperature and pressure error correlation functions decay to negative values before returning to zero at longer distances. For SWH on the scales of interest here, this is not generally the case, so a simpler form for the correlation function can be considered by removing the cosine dependancy. In addition, the constraint that $\rho(r = 0) = 1.0$ is included. This simplified function is, therefore,

$$\rho(r,\theta) = \exp\left[-\frac{d}{a_3}\right], \tag{8}$$

with d given by Eq. (7). This results in elliptical contours (which seems reasonable considering Fig. 2), with the parameter a_1 related to the eccentricity (e) of the ellipses, a_2 giving the tilt of the ellipse, and a_3 defining a length scale (or a rate of decay).

The procedure used to find the best estimate for a_i was a Numerical Algorithms Group (NAG) FORTRAN library minimization subroutine. For details, see Greenslade (2004). Figure 3 shows contours of the analytic functions that were found to be the best fit to the correlations shown in Fig. 2. In this case, the best-fit values for the parameters are shown in Table 2. Figure 3 and Table 2 demonstrate that the thinning of the model data by using only every fifth grid point has only a minor effect on the results.

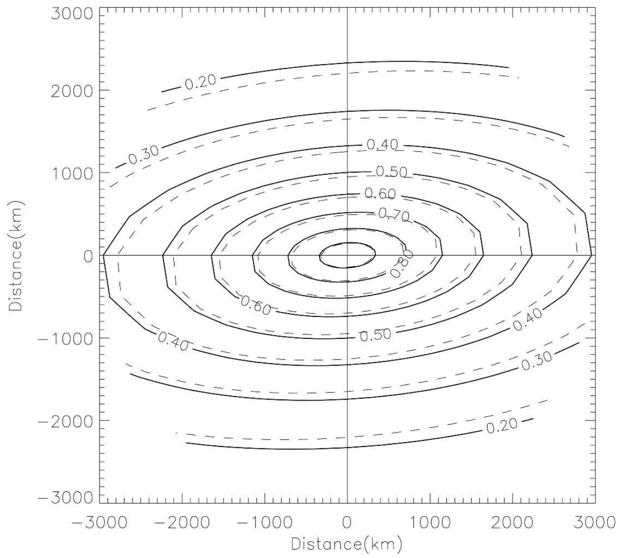

FIG. 3. Best-fit analytic surfaces for the correlation functions shown in Fig. 2. The solid line is for the case of all model grid points and the dashed line for the case using every fifth point. Note that the contour levels for the solid and dashed lines are the same.

In addition to the anisotropic (two-dimensional) fitting, the correlations were fit to isotropic functions. Candidate functions were Gaussian, that is,

$$\rho(r) = \exp\left[\frac{-r^2}{2a_1^2}\right], \tag{9}$$

and a second-order autoregressive function (SOAR), that is,

$$\rho(r) = \left(1 + \frac{r}{a_1}\right) \exp\left[-\frac{r}{a_1}\right]. \tag{10}$$

Figure 4 shows the same correlations as in Fig. 2b but as a function of distance alone, along with the best-fit isotropic functions. Overall, it was found that the SOAR function was a better fit to the correlations than the Gaussian function; that is, the mean square error was smaller. For the remainder of this section, only the SOAR function is considered.

The best-fit value for the parameter a_1 in this case

TABLE 2. Values of a_i for the surfaces shown in Fig. 3.

	a_1	a_2	a_3
All points	1.50	86.0	2168.9
Every fifth point	1.50	85.0	2052.6

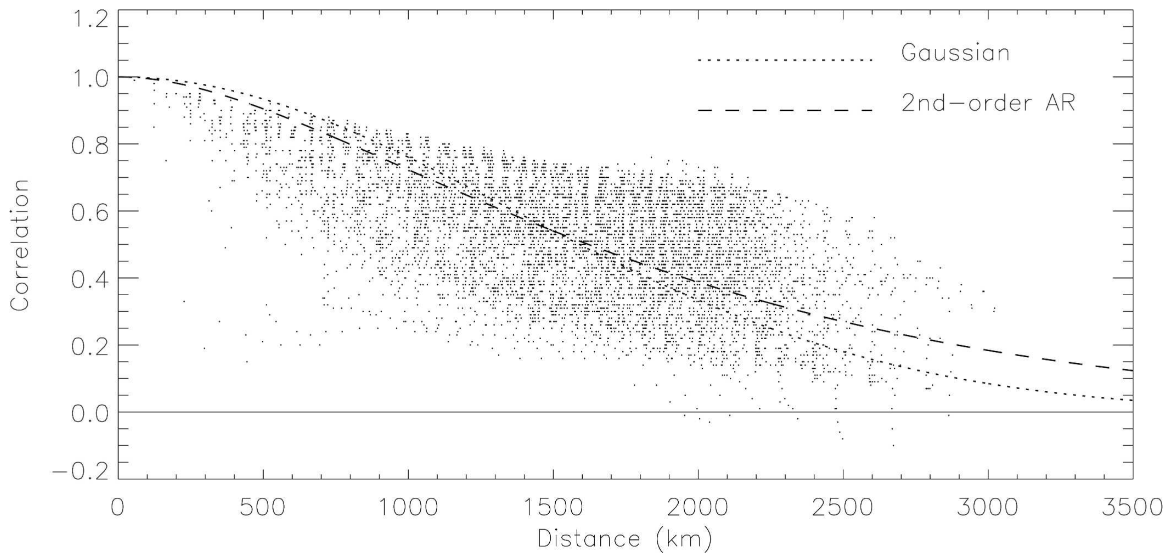

FIG. 4. Isotropic correlations for the same area and time period as in Fig. 2b. The dotted line is the best-fit Gaussian curve and the dashed line is the best-fit autoregressive curve.

(i.e., the value of a_1 for the dashed curve in Fig. 4) was found to be $a_1 = 966$ km. This is, therefore, the length scale L of the model anomaly correlation in this region.

c. *Regional effects*

Anomaly correlations were calculated as described above for 20° boxes at 10° intervals over the entire globe for two 3-month time periods: 1 July–30 September 1998 and 1 January–31 March 1999. The best-fit analytic functions for both the isotropic and anisotropic cases were determined for each box.

1) ISOTROPIC CASE

Figure 5 shows how the isotropic correlation length scale, that is, a_1 in Eq. (10), varies over the globe for these two time periods. It can immediately be seen that the length scale varies quite significantly in space. This indicates that the modeled SWH is not strictly homogenous over the globe.

In Fig. 5a, which represents the Southern Hemisphere (SH) winter case, the longest scales are found in the northern Indian Ocean (Arabian Sea) and in the eastern equatorial Pacific. Longer scales imply that the model deviates from the climatology on a large spatial scale. This means that areas of anomalously high or low SWH are large during this time period. The area of long length scales in the Arabian Sea is associated with the Indian monsoon. From May to September, winds in this region blow persistently from the southwest, and so during this time period the fetch for this area is relatively long, stretching along the east African coast. Thus, an area of persistently high SWH develops in the Arabian Sea (Young 1999). The size of the correlation length scales in Fig. 5a reflects this.

The shortest length scales (<500 km) can be seen on the western boundaries of the ocean basins and also in the Southern Ocean in a band of short scales around 40°S. The short scales in this area reflect the spatial scale of the storm areas that propagate from west to east along this latitude band.

For the SH summer case (Fig. 5b), the length scales increase in the northern Atlantic Ocean and the eastern Pacific (cf. Fig. 5a). The area of long length scales in the northern Indian Ocean disappears because the winds are predominantly from the northeast during this time period.

2) ANISOTROPIC CASE

Figures 2 and 3 indicate that the anomaly correlation may not be isotropic. After fitting the analytic function, an indication of the anisotropy of a particular correlation function can be obtained from inspecting just one contour level, because each contour holds the same information on the eccentricity and tilt of the ellipse (see, e.g., Fig. 3). Figure 6 shows the 0.5-level contour of the anomaly correlations for each 20° box over the globe for each time period. Note that the axis length of each ellipse is defined in kilometers and then plotted on the latitude–longitude grid. This means that the differences in the size of the ellipses seen in Fig. 6 are real and not simply an artifact of the map projection. The relative size of the ellipses corresponds well to the isotropic

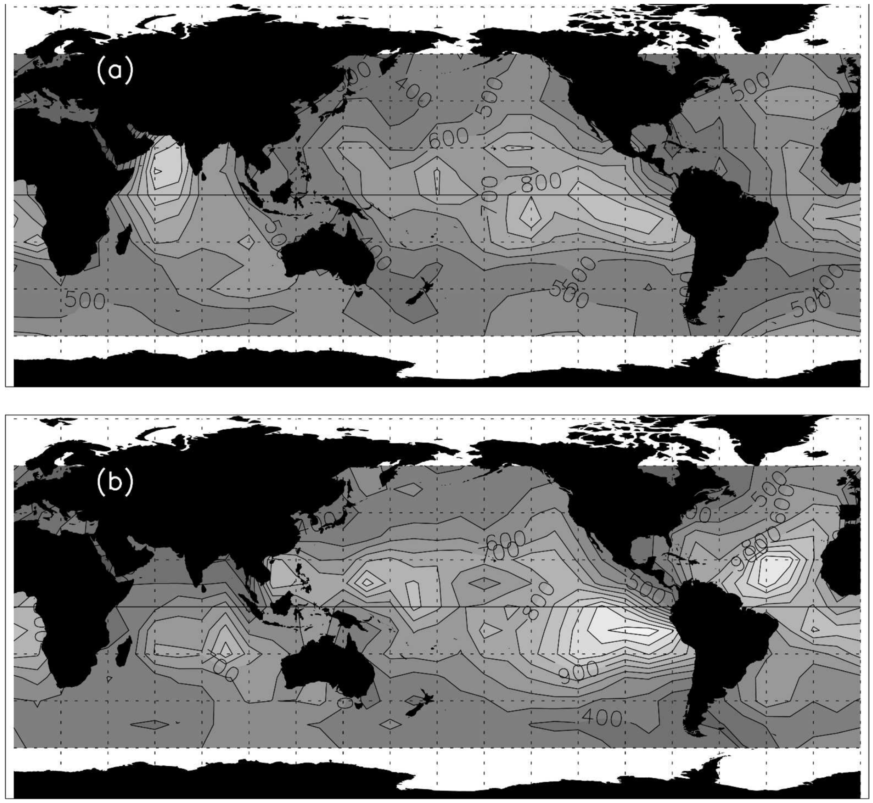

FIG. 5. Isotropic anomaly correlation length scale (km) for modeled SWH over the globe for 20° boxes at 10° intervals for (a) Jul–Sep 1998 and (b) Jan–Mar 1999.

correlation scales seen in Fig. 5. In particular, note that the smallest ellipses for both time periods occur around 40° and 50°S, corresponding to the band of short isotropic length scales at these latitudes. The largest ellipses occur in the eastern Pacific for both time periods, and also in the North Atlantic for January–March 1999 and in the Arabian Sea. The angle of the ellipses in this region confirms that the structure of the anomalies is due the southwesterlies of the Indian monsoon.

Overall, it can be seen that the anomaly correlations are generally not isotropic. For July–September 1998, the most isotropic regions are in the northwest portions of the ocean basins, and along the southernmost latitude band. Where the ellipses are not isotropic, they are mostly elongated in the east–west direction. In the Northern Hemisphere (NH), these are generally tilted toward the northeast, and in the SH, they are tilted toward the southeast. Areas for which the anomaly correlations are particularly anisotropic are the Indian Ocean to the west of Australia and the Pacific Ocean to the west of South America. If the background errors have the same structure as the model anomalies shown here, then this would have implications for the data assimilation schemes that currently use simple isotropic correlation functions. Figure 6b shows a generally similar pattern to that of the earlier time period. Some major differences are that the western subtropical Pacific has increased anisotropy, and the structure of the correlation functions in the northern Indian Ocean is significantly different.

These results show a similar pattern to that remarked upon by Seaman and Gauntlett (1980). In that work, four studies of the directional dependence of wind correlation coefficients in different geographical regions were examined. It was shown that the major axis of the correlation function was rotated toward the northeast in the NH and the southeast in the SH. In the case of SWH anomalies, the directional distribution of the anomaly correlation functions can be attributed to the predominant direction of propagation of wave systems in different regions. These, in turn, are results of the predominant surface wind patterns. For example, the ellipses in the Pacific Ocean between approximately 30°N and 30°S tend be aligned with the trade winds—the southeast trades in the SH and the northeast trades in the NH. From 40° to 50°S the ellipses are more zonally aligned, corresponding to the persistent westerly winds at these latitudes. Alternatively, the directional

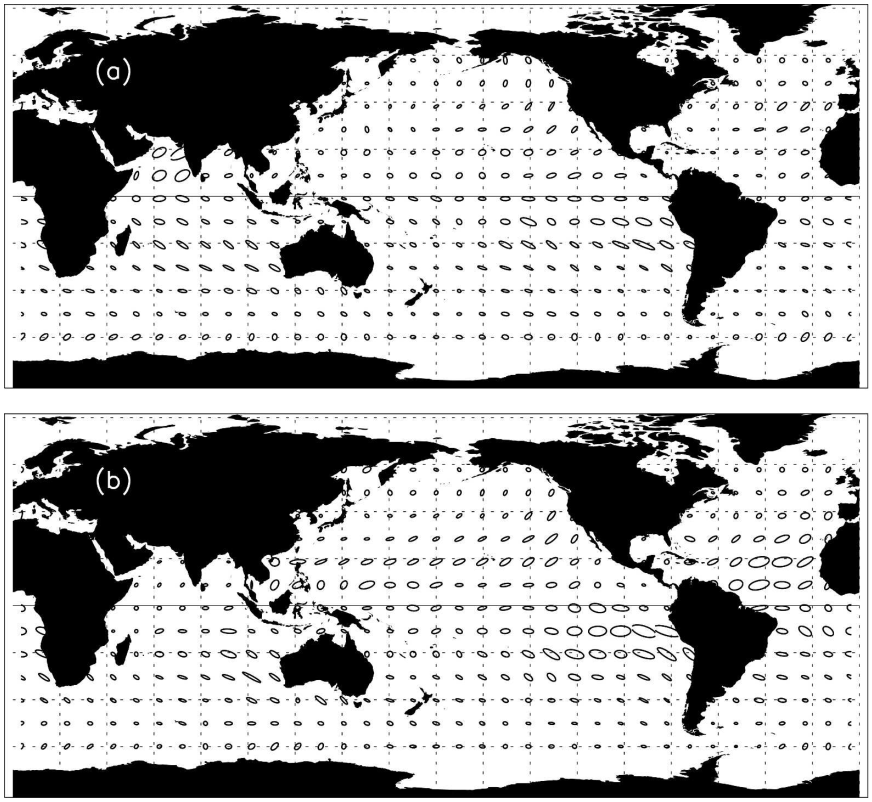

FIG. 6. The 0.5-level contour of the best-fit anisotropic correlation function for modeled SWH over the globe for 20° boxes at 10° intervals for (a) Jul–Sep 1998 and (b) Jan–Mar 1999.

distribution of the anomaly correlation functions could be a result of the propagation of swell. Swell generated by storm systems in the Southern Ocean, for example, tends to propagate toward the northeast. The ellipses in the southeastern Pacific and central Indian Oceans are, therefore, generally aligned with their short axes in the swell direction, and long axes perpendicular to the direction of propagation of the swell.

5. Anomaly correlations from simulated altimeter data

In this section, the ability of simulated altimeter data to obtain the same results as those from the full gridded model output is examined. Altimeter ground tracks (i.e., latitude, longitude, and time) were created for a satellite with an altitude of approximately 788 km and an orbital inclination of 108°. These are the parameters of the *Geosat* mission. The repeat period of the *Geosat* altimeter is 17.05 days. This means that within a 3-month period, each ground track will be sampled 5 or 6 times. The orbital period of the satellite, that is, the time between subsequent ascending (or descending) equator crossings, is approximately 100 min. The along-track spacing of observations was set to be 20 km.

A set of ground tracks was generated for every 20° box and for each of the 3-month periods described above. For each box, the background field (i.e., the model climatology) and the 6-hourly model fields were interpolated to the simulated altimeter observation locations. Bilinear interpolation was required for the background fields (two space dimensions) and trilinear interpolation for the 6-hourly model fields (two space dimensions plus time). Figure 7a shows an example of a model background field, and in Fig. 7b that field is interpolated to the altimeter observation locations and recontoured. Model grid points and altimeter ground tracks (all observations within the 3-month time period) are shown. In can be seen that the altimeter data are able to represent the background fields very well.

a. Correlation computations

The calculation of error correlations from the simulated altimeter data is complicated by the fact that an altimeter dataset represents a time series and few of the observations can be considered to be simultaneous. To

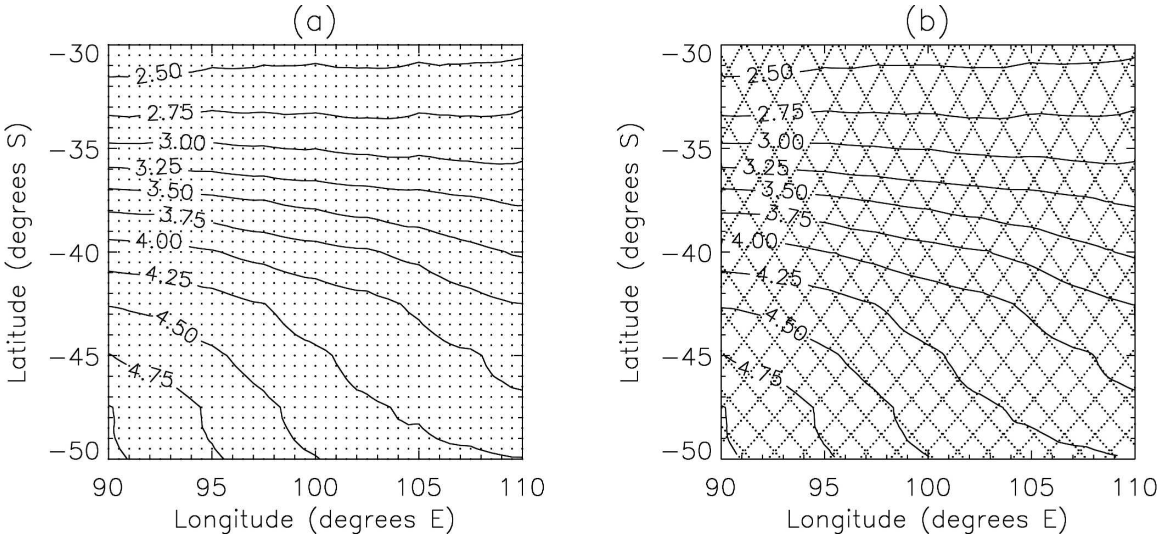

FIG. 7. (a) An example of a model background field (dots represent model grid points), that is, a climatological SWH field and (b) the same field after sampling the model output at simulated *Geosat* altimeter observations locations (dots) and recontouring.

calculate a correlation between two observation locations j and k according to Eq. (4), there are two criteria that must be satisfied.

1) There must be simultaneous observations at each location. This is easily satisfied for the model fields, but for altimeter data, there are *no* observations that are simultaneous. However, simultaneous can be defined as occurring within a short enough time period (say, t_{max}) so that the field of interest does not vary significantly. This is discussed further below.
2) Not only must criterion 1 be satisfied, but it must be satisfied more than once within the time period of interest. If there is only one observation at each location, then R_{jk} reduces to the trivial case of $R_{jk} = 1$. This is one of the reasons that a time period of 3 months was chosen, as opposed to a shorter time period.

The temporal distribution of the *Geosat* altimeter observations within a 20° box on the earth's surface near the equator is fairly complex. For a 20° box, one overpass takes approximately 6 min. If this is, say, an ascending pass, then the time to the next observation within the box depends on whether the next ascending pass falls within the box or not. If it does, then the time to the next overpass is approximately 100 min (i.e., the orbital period). If the next ascending pass falls outside the box, then the next observation falling within the box will come from a descending pass. This will occur after the earth has gone through half a rotation period (i.e., 12 h), and so the time to the next observation within the box will be either approximately 10.8 or 12.5 h.

The combination of the two criteria outlined above and the altimeter sampling pattern means that if $t_{max} =$ 15 min, then the set of data pairs between which correlations can be calculated consists of only along-track combinations. This severely limits the amount of directional information on the correlations. In other words, there is no information on correlations in the zonal or meridional directions, but only in the direction of the ground tracks. However, if t_{max} is extended to 2 h, then this allows the inclusion of prior or subsequent same-direction ground tracks. This then provides additional information in the zonal direction.

The disadvantage of extending to $t_{max} = 2$ h is that there is the possibility that the SWH field will have been altered within the 2-h period, which would corrupt the correlation calculations. Situations in which the SWH field would be expected to alter the most rapidly are those in which the wind speed and/or wind direction changes abruptly. The dimensionless time scale $\tilde{\tau} = g\tau/U_{10}$, of the response of the mean wave direction to a change in wind direction can be expressed as (Günther et al. 1981)

$$\tilde{\tau} = \chi^{-1}\nu^{-2}, \tag{11}$$

where χ is a constant and the dimensionless peak frequency is $\nu = f_p U_{10}/g$. Observational studies (see Komen et al. 1994) have found χ to range from 0.12×10^{-2} to 0.57×10^{-2}. Using typical open-ocean values of $f_p =$ 0.1 Hz and $U_{10} = 10$ m s^{-1}, this gives response time scales ranging from approximately 5 to more than 22 h. This indicates that 2 h is a reasonable time period dur-

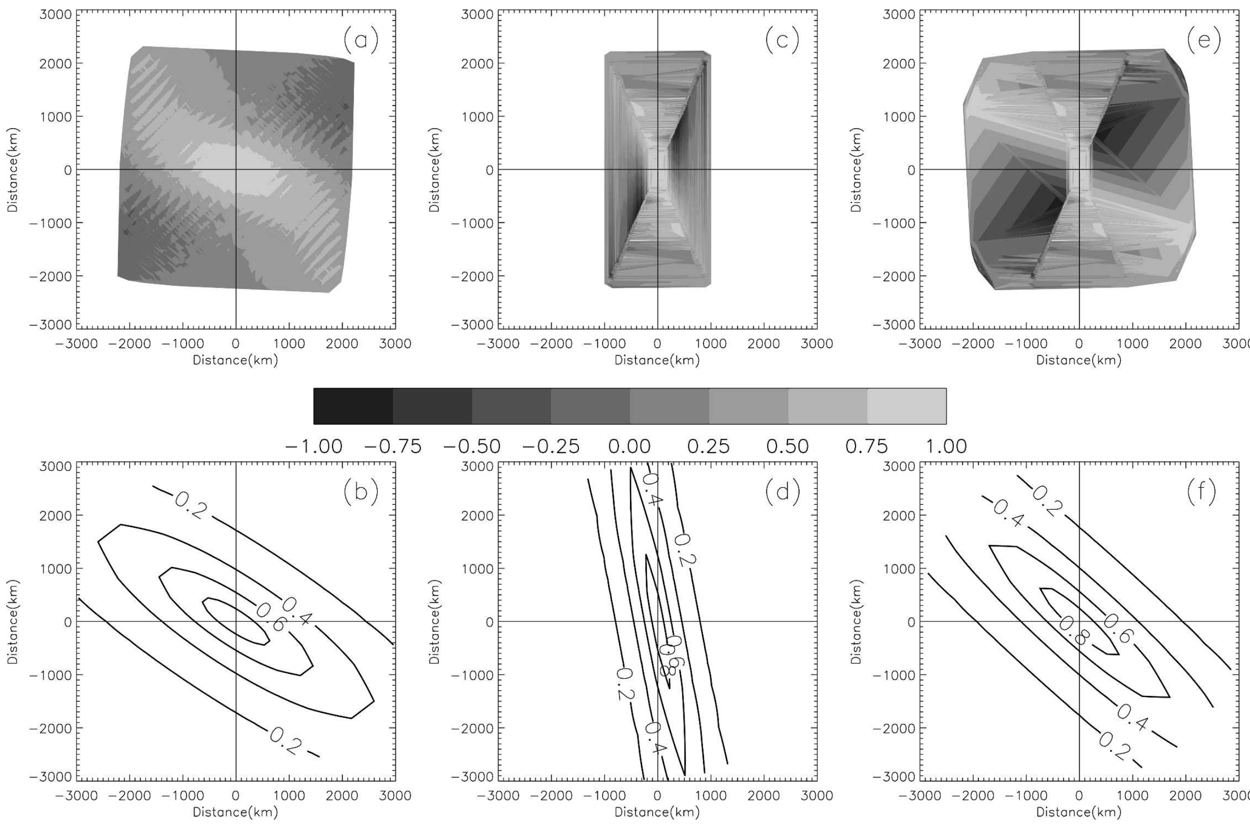

FIG. 8. (a) Model anomaly correlations for a 20° box centered at 20°S, 70°E for Jul–Sep 1998. (b) Best fit to the correlations shown in (a). (c) Same as (a), but using data from simulated altimeter ground tracks and calculating correlations with t_{max} = 15 min. (d) Best fit to the correlations shown in (c). (e) Same as (a), but using data from simulated altimeter ground tracks and calculating the correlations with t_{max} = 2 h. (f) Best fit to the correlations shown in (d).

ing which it can be assumed that the SWH field will not change significantly.

Following Eq. (4), error correlations $R_{jk} = \rho(r, \theta)$ were calculated from the simulated altimeter data for all 20° boxes over the globe at 10° intervals for both t_{max} = 15 min and t_{max} = 2 h. For these calculations, B_i is the value of the model climatology interpolated to the altimeter observation locations, as represented in Fig. 7 and the O_i are the simulated altimeter observations. The time average is the average over the number of time levels for which observations occur at both locations j and k. For the anisotropic case, the correlations are averaged into bins of 1-km radius and 1° angle, and then are fitted to the same analytic functions that are used for the model anomaly correlations, that is, Eq. (8). For the isotropic case, the correlations are averaged into 10-km bins and then fitted to the SOAR curve given by Eq. (10).

Figure 8a shows an example of the model anomaly correlations for the 20° box centered at 20°S, 70°E in the central Indian Ocean. Figures 8c and 8e show the equivalent error correlations for the altimeter-sampled case for the two different values of t_{max}. The best-fit analytic anisotropic surfaces are shown in the bottom panels. Table 3 shows the values of a_i for the surfaces shown in these panels.

Consider first the altimeter case with t_{max} = 15 min, that is, Figs. 8c and 8d. The first point to note is that, as opposed to the full-model anomaly correlations, the correlations using the simulated altimeter data cannot be described well by an elliptical function. The only information on the value of the correlation function in this case is from along-track data pairs. There is no information available on the value of the correlations in the east–west direction. Some basic features of the full-model anomaly correlations are still evident, however.

TABLE 3. Values of a_i for the surfaces shown in Figs. 8b, 8d, and 8f.

	a_1	a_2	a_3
Model	1.92	123.4	1737.1
Alt t_{max} = 15 min	3.46	169.4	1679.6
Alt t_{max} = 2 h	2.32	132.2	1908.3

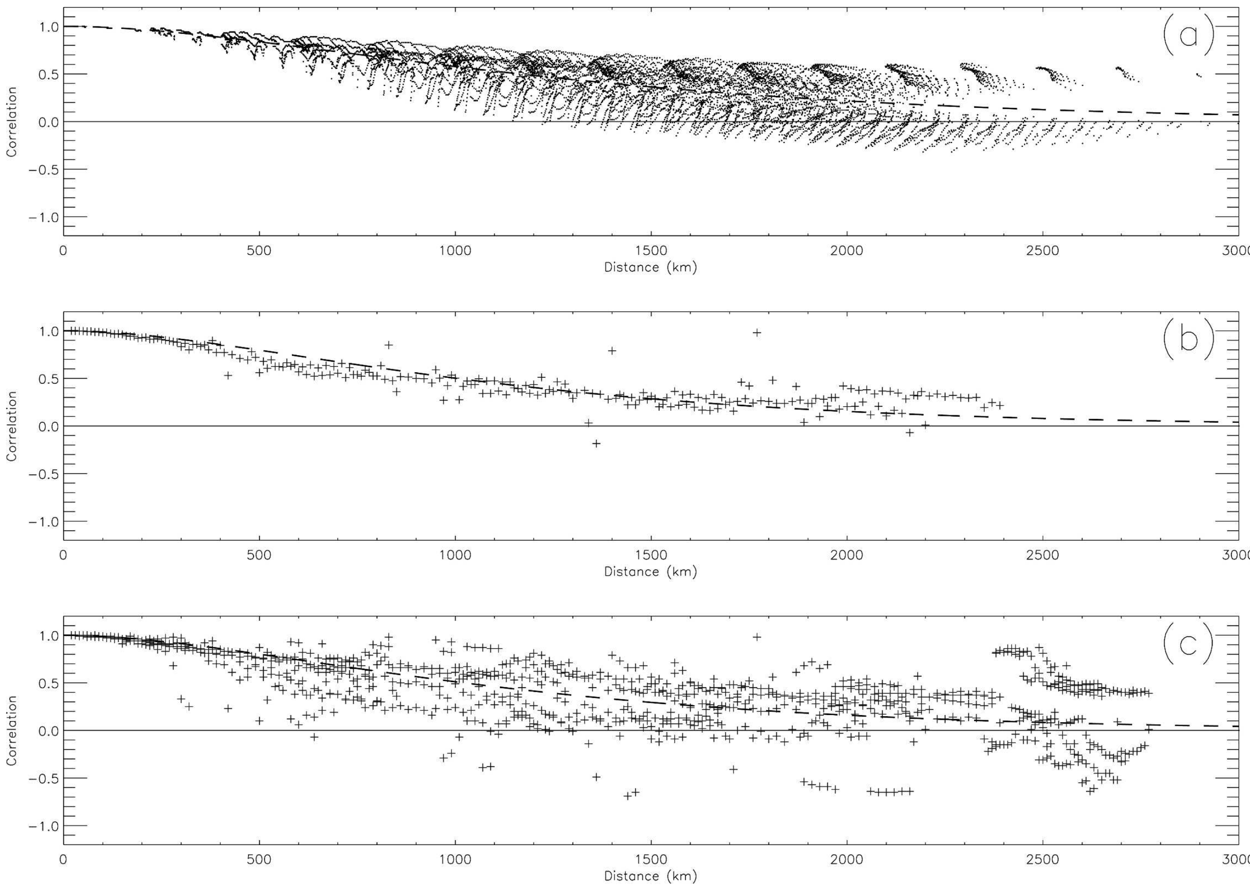

FIG. 9. Same as Fig. 8, but for isotropic fitting. The dashed line represents the best-fit autoregressive function. (a) Correlations from model output. (b) Correlations from simulated altimeter data with $t_{max} = 15$ min. (c) Correlations from simulated altimeter data with $t_{max} = 2$ h.

The correlations are generally higher at shorter scales. In addition, the correlations in the northeast direction are lower than those in the southeast direction. This leads to an analytic function for which the main features are similar to those of the model anomaly correlations. In particular, the tilt of the ellipse is in the correct direction and taking a slice from the center to the top-right corner will lead to a similar decay rate. (i.e., the contours in that quadrant are in approximately the right place). However, note that the values for the parameters a_1 and a_2 are both far too large.

Figures 8e and 8f show how the correlations change with the inclusion of subsequent/prior ground tracks, that is, using $t_{max} = 2$ h. The fitted analytic function is now considerably closer to the analytic model anomaly correlation function, and this is reflected in the a_i values. Although the value of a_3 is now slightly further away from the truth, a_1 and a_2 are quite close (within approximately 15%) to those of the model anomaly correlations.

Figure 9 shows the equivalent plots for the isotropic fitting, along with the best-fit autoregressive curves. The regular curved pattern seen in the full-model anomaly correlation in Fig 9a arises from the use of only every fifth model grid point in the correlation calculations. This is analagous to the "banded" effect seen in Fig. 2b. Note the two distinct tails in the model anomaly correlations, representing the higher values in the southeastern quadrant and lower values in the northeastern quadrant of the anisotropic correlations. With the $t_{max} = 2$ h case, the extra correlation values at large values of r (i.e., correlations between observations from different ground tracks) are not, in general, close to those of the model, but they do force the fitted curve to be closer to that of the full-model anomaly correlation function. This can be seen in the resulting values of L [i.e., a_1 in Eq. (10)], shown in the first column of Table 4.

The full-model anomaly correlation length scale is defined here to be the true length scale L. For this particular example, $L = 692.9$. The length scale, as obtained from simulated altimeter data with $t_{max} = 2$ h, L_{alt-2h}, underpredicts the true length scale by approxi-

TABLE 4. Isotropic length scales for the correlations shown in Fig. 9.

	L
Model	692.9
Alt t_{max} = 15 min	597.4
Alt t_{max} = 2 h	607.9

mately 12%. This is fairly typical and will be discussed further in section 6.

b. Regional effects

As in the case of the modeled wave fields, correlations were calculated for all 20° boxes over the globe from simulated altimeter data for the same 3-month time periods as considered in the previous section. In this section, only the case with t_{max} = 2 h is considered, because it has been shown to provide results that are closer to those of the true correlations. The case with t_{max} = 15 min will be returned to in section 6.

1) ISOTROPIC CASE

Figure 10 shows how L_{alt_2h} varies over the globe for the two 3-month time periods. Comparing Fig. 10a to Fig. 5a, it can be seen that most of the main features of the global distribution are evident. In particular, the longest scales occur in the eastern Pacific and northern Indian Ocean, and a band of short scales occurs in the Southern Ocean. In addition, the pattern in the Atlantic Ocean (north and south) is very similar in the two plots.

Figure 10b is the same as Fig. 10a, but for the second 3-month time period. Again, the main features of Fig. 5b can be seen here. In particular, the longest scales are in the eastern Pacific and northern Atlantic, while the long scales in the northern Indian Ocean disappear. Similarly to the full-model anomaly correlations, length scales in the western Pacific lengthen compared to the earlier time period. This suggests that the simulated altimeter data are able to capture some of the seasonal variability in the true correlations. A quantitative analysis of the relationship between the true length scales in Fig. 5 and the length scales from the simulated altimeter data in Fig. 10 is given in section 6.

2) ANISOTROPIC CASE

The fitting of anisotropic functions to the correlations from the simulated altimeter data is considered in this section. Because of the limited range of angles of

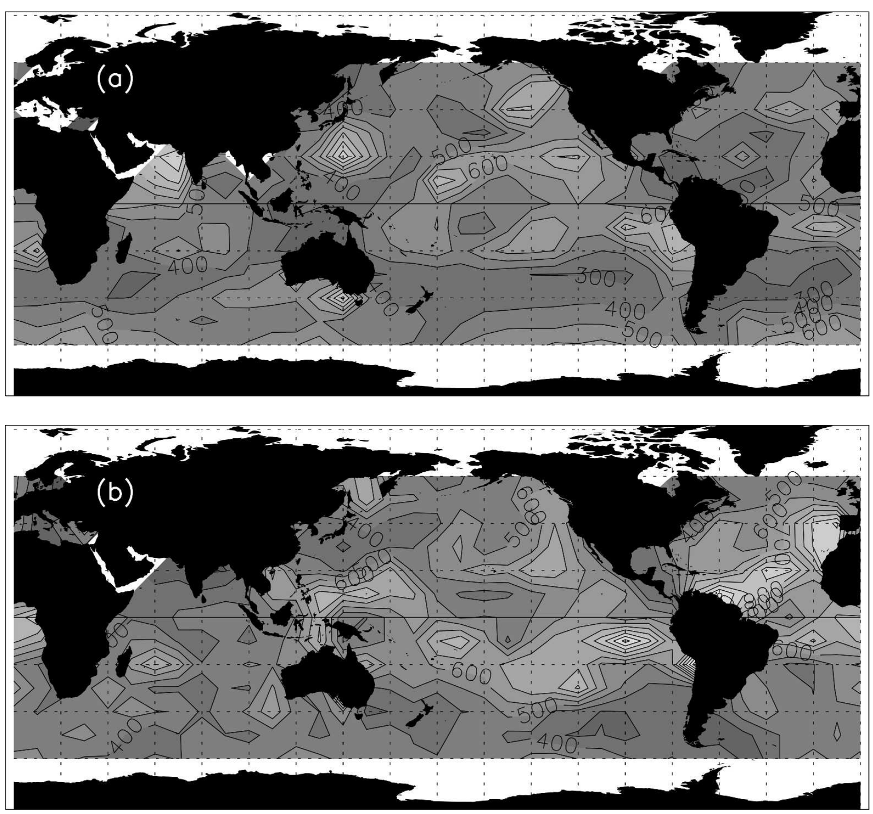

FIG. 10. Isotropic correlation length scale (km) over the globe from simulated altimeter data for 20° boxes at 10° intervals for (a) Jul–Sep 1998 and (b) Jan–Mar 1999.

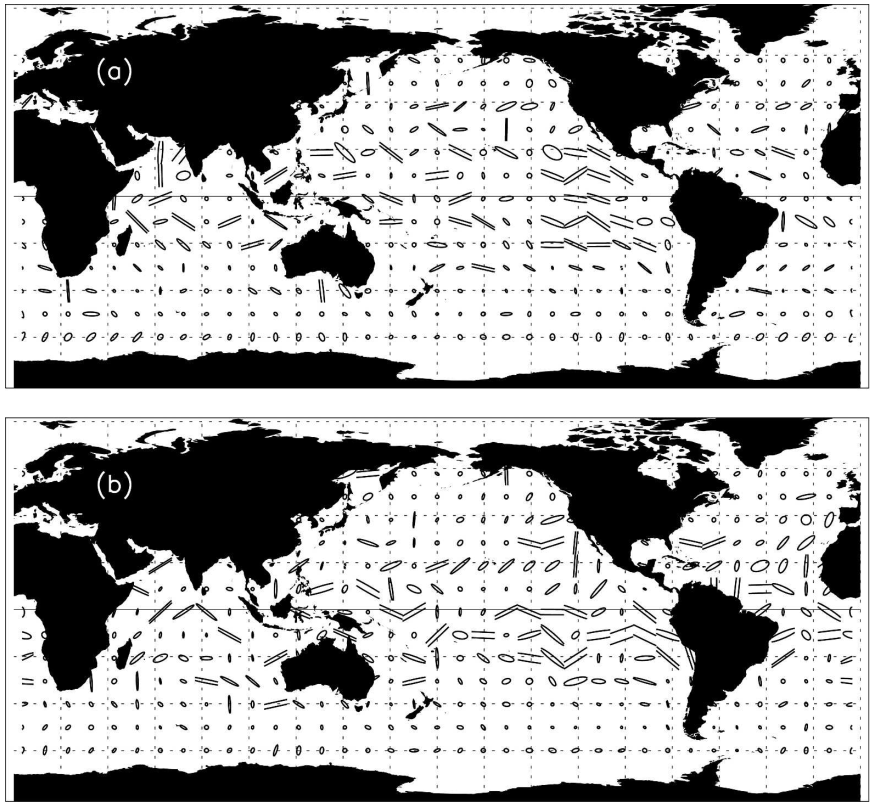

FIG. 11. Same as Fig. 6, but for correlations calculated from simulated altimeter data with t_{max} = 2 h: (a) Jul–Sep 1998 and (b) Jan–Mar 1999.

the altimeter sampling pattern, one might anticipate difficulties in obtaining functions similar to those obtained from the complete model dataset. However, it has been shown that by considering t_{max} = 2 h, the amount of information available in the zonal direction can be increased. Figure 11 shows the 0.5-level contour of the error correlations from simulated altimeter data (using t_{max} = 2 h) for each 20° box. Comparing these with Fig. 6, it can be seen that there are many locations where the ellipses are very different to the model ellipses. On the other hand, there are some encouraging similarities between the plots.

Compare the plots for the first time period, that is, Figs. 6a and 11a. For both cases, the eastern Pacific has a large number of highly eccentric ellipses. South of the equator, these are generally tilted in the right direction. Poleward of 40°N and 40°S the comparison is quite good, that is, the size of the ellipses is approximately correct and they are generally isotropic or more meridionally aligned. The improved performance of the altimeter sampling pattern at higher latitudes is partly a result of the higher density of observations in these regions, and partly a result of their distribution. The convergence of meridians results in the satellite ground tracks becoming more east–west aligned at higher latitudes. This means that at higher latitudes, the data pairs for the correlation calculations occur over a much larger range of angles, and so there is more information available on the correlations in the east–west direction.

For the second time period (Figs. 6b and 11b) the impact of the altimeter sampling pattern is very similar in terms of the comparison with the anisotropic anomaly correlation field.

3) ASCENDING AND DESCENDING TRACKS

Another possible method to obtain anisotropic correlations from the altimeter data is to examine the along-track correlations from ascending and descending ground tracks separately. In this section, this possibility is explored. Because only along-track data are used, the set of data pairs between which correlations are calculated within a 3-month period will be identical whether t_{max} = 2 h or t_{max} = 15 min is used. For each 20° box, a set of correlations exists for the simulated altimeter data as a function of distance and angle (see, e.g., Fig. 8c). These correlations are divided into two groups. Correlations between data pairs along ascending tracks are those for which the angle between the

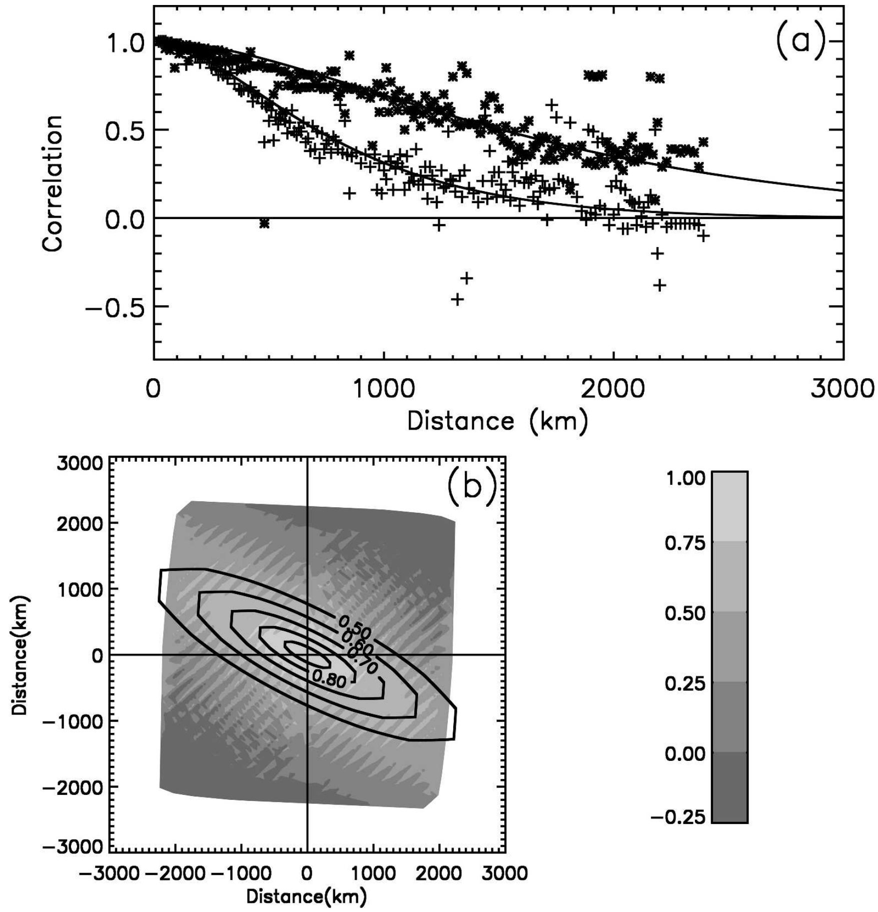

FIG. 12. (a) Correlations from simulated ascending ground tracks (asterisks) and descending ground tracks (crosses) for the box centered at 20°S, 140°W. (b) Anisotropic model anomaly correlations for the same box.

two observation locations is greater than 90°. Similarly, correlations along descending tracks are those for which the angle between the two observation locations is less than 90°. The "ascending" angle and the "descending" angle are defined to be the average angle between all data pairs within each group. The isotropic fitting procedure is applied for the correlations between data pairs along ascending tracks and the correlations between data pairs along descending tracks separately (after averaging into 10-km bins). This produces two length scales—one from data pairs along ascending tracks alone, L_{asc}, and one from data pairs from descending tracks alone, L_{desc}—and two associated angles.

Figure 12a shows correlations from the ascending and descending tracks for a box in the western Pacific centered at 20°S, 140°W, and Fig. 12b shows the true anisotropic anomaly correlation for the same box. This method shows promising results. The anomaly correlations are clearly higher in the quadrant of the ascending tracks than that of the descending tracks, and this can be seen in Fig. 12a, where L_{asc} = 900 km and L_{desc} = 420 km.

Figure 13 shows contour plots of L_{asc} and L_{desc} over the globe for the time period of July–September 1998. Comparing this to the actual anisotropic model anomaly correlations (Fig. 6a), it can be seen that many of the major features of the global distribution are replicated. For example, in the eastern Pacific south of the equator, the anomaly correlations are generally tilted toward the southeast, and are more closely aligned with the ascending ground tracks than the descending ground tracks. And, indeed, L_{asc} is generally higher in this region than L_{desc}. Conversely, in the northeastern Pacific, L_{desc} is generally higher than L_{asc}, and in this region the ellipses are tilted at an angle that is closer to the angle of the descending ground tracks.

It is possible to construct an ellipse from these two length scales and the two angles. The major axis of the ellipse must be defined to lie in the direction of either

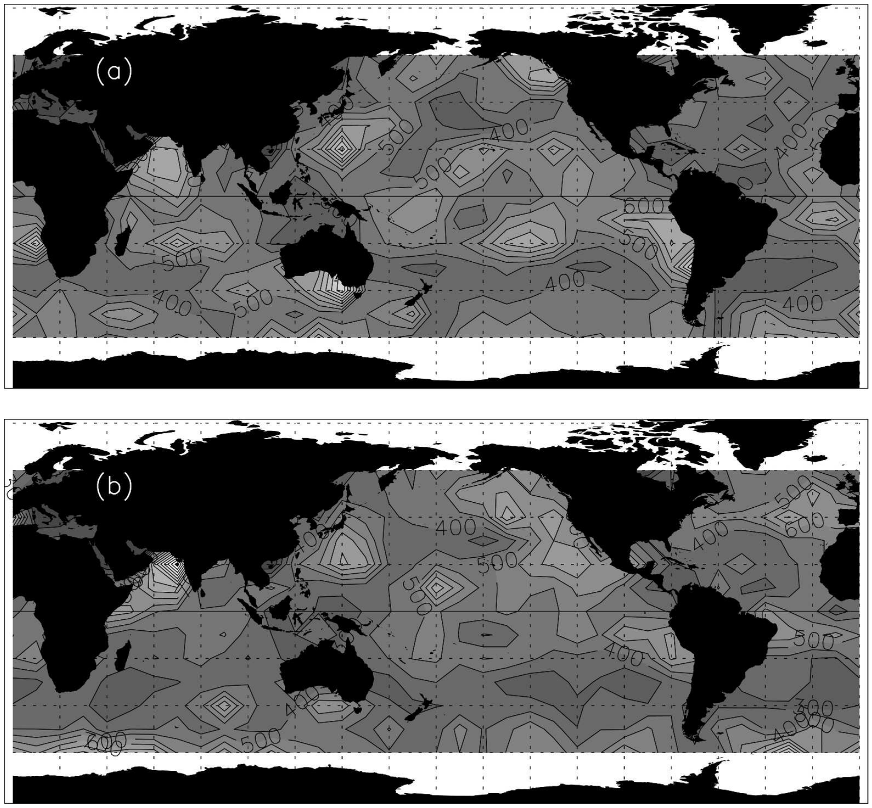

FIG. 13. (a) Contours of L_{asc} (km) for Jul–Sep 1998 and (b) L_{desc} (km) for the same time period.

the ascending ground tracks or the descending ground tracks. This means that none of the ellipses will be aligned east–west or north–south. However, in this section it has been shown that it should be possible to obtain at least *some* information on ellipse orientation from the ascending/descending method. Figure 14 shows the anisotropic correlations constructed in this manner. Again, comparing these to Fig. 6, it can be seen that although there are serious deficiencies, some of the major features of the global distribution of the anisotropic anomaly correlations are evident. Note, in particular, the large ellipses in the northern Indian Ocean during July–September 1998. In the more central parts of the Indian Ocean there is a tendency for the ellipses to be aligned toward the southeast. In addition, the size of the ellipses in the North Atlantic Ocean is considerably larger during January–March 1999 than during July–September 1998, and they are aligned in the correct direction.

These results imply that there is potential to obtain information on anisotropic error correlations from altimeter data. It is not known whether the incorporation of anisotropy in a background error correlation function would provide any improvement over a simple isotropic correlation function. This will be explored in future work.

6. Further issues

In this section, the isotropic correlation length scales from the simulated altimeter data are examined further.

a. Isotropic corrections

An appropriate correction to L_{alt} is now developed. The optimal method would provide a consistent correction to L_{alt} (by minimizing variable errors), rather than a method that produces values closest to the true L (by minimizing the bias), so it is worthwhile here to examine the estimates of L_{alt_15min} as well as those of $L_{alt–2h}$.

Figure 15 shows the difference between L and $L_{alt–2h}$ as a percentage of L for the two time periods. It can be seen that over most of the ocean, the altimeter sampling pattern causes the length scale to be underestimated. The areas where L is underestimated by the largest amount are generally near the centers of ocean basins, while areas where the altimeter overestimates the

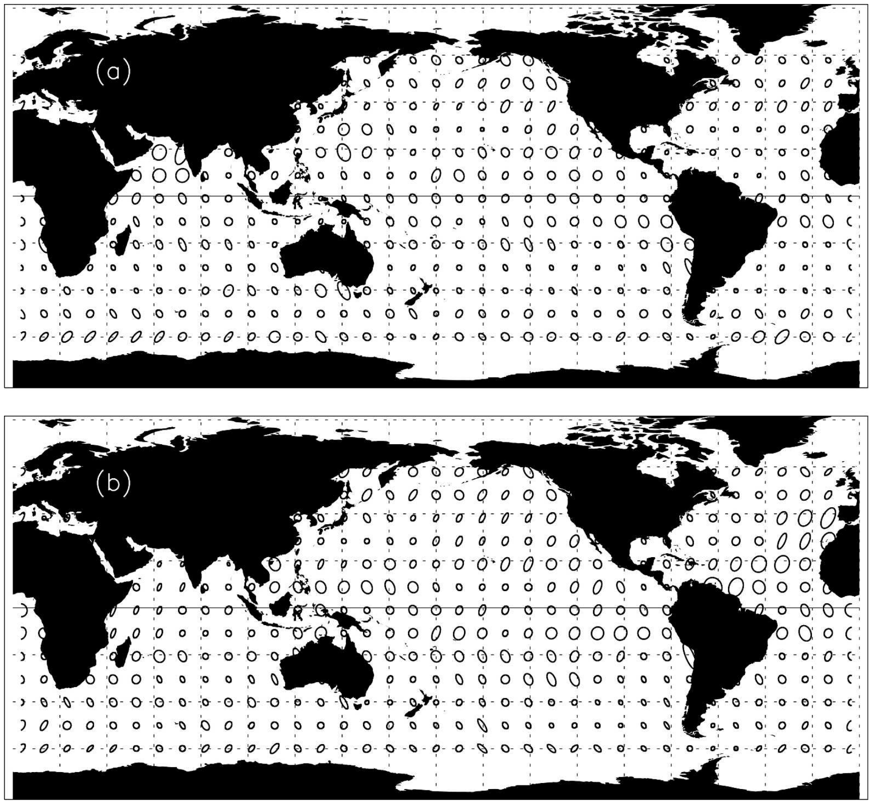

FIG. 14. Anistropic anomaly correlations from ascending and descending tracks for (a) Jul–Sep 1998 and (b) Jan–Mar 1999.

length scale are generally near the coast, or along the southernmost latitude band. A similar pattern appears for both time periods, indicating that although the true anomaly correlation length scales vary seasonally, the effect of the altimeter sampling pattern is consistent in time.

Figure 16 shows the isotropic correlation length scales calculated from the simulated *Geosat* data with $t_{\max} = 15$ min. Comparing this figure to Fig. 10 it can be seen that, although the magnitude of the length scales varies considerably, the regional variability is very similar whether $t_{\max}$ is 15 min or 2 h.

In addition to $L_{\mathrm{alt-15min}}$ and $L_{\mathrm{alt-2h}}$, a third method to obtain isotropic length scales is also examined here. This third length scale is obtained from the method considering ascending and descending tracks separately. Specifically, L_{ad} is defined as

$$L_{\mathrm{ad}} = \frac{L_{\mathrm{asc}} + L_{\mathrm{desc}}}{2}. \tag{12}$$

It was found that this produced a global distribution of isotropic length scales that is very similar to the global distribution of $L_{\mathrm{15-min}}$, so it is not shown here.

Overall differences between $L_{\mathrm{alt-2h}}$ and L, $L_{\mathrm{alt-15min}}$ and L, and L_{ad} and L are now considered (including results from both time periods). Table 5 shows the mean differences and standard deviations for each method of calculating L. These figures suggest that using $L_{\mathrm{alt-2h}}$ appears to be the best option: the overall bias (km) is lowest (i.e., $\overline{L_{\mathrm{alt\_2h}}} = \overline{L} - 70.7$ km) and, more importantly, the standard deviation is the smallest. In terms of a percentage of L, the mean difference for $L_{\mathrm{alt-2h}}$ is 10.3%, suggesting that a possible course of action might be to calculate $L_{\mathrm{alt-2h}}$ and then increase it by 11.5% to obtain the best estimate of the true correlation length scale. (If $L_{\mathrm{alt-2h}} = 89.7\%\ L$, then $L = 111.5\%\ L_{\mathrm{alt-2h}}$.) Note that the difference between the three methods is not substantial, particularly in terms of the standard deviation.

b. The impact of anisotropy on isotropic length scales

The amount by which the altimeter underestimates (or overestimates) the isotropic correlation length scale should be a function of the shape of the true anisotropic correlation function. If the anomaly correlation is iso-

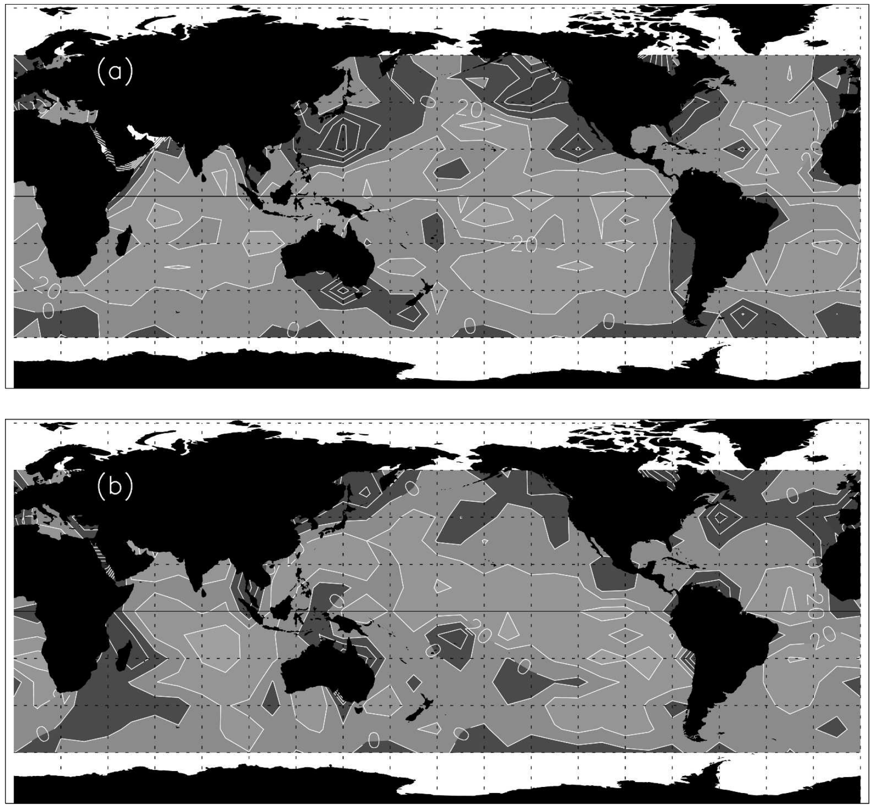

FIG. 15. Difference (as a percentage of the full-model anomaly correlation length scale) between Fig. 10 and Fig. 5 for (a) Jul–Sep 1998 and (b) Jan–Mar 1999. Light shaded areas are where $L_{\mathrm{alt-2h}} < L$ and dark shaded areas are where $L_{\mathrm{alt-2h}} > L$.

tropic, then the true correlation length scale is the same in all directions, and the limited directional sampling of the surface by the altimeter should not have any impact on the estimate of the length scale. As the correlation function becomes more anisotropic and the ellipses become more eccentric, then the underestimation of L by the altimeter becomes dependent upon the angle between the altimeter ground tracks and the major axis of the ellipse.

This can be examined more closely by comparing the difference between $L_{\mathrm{alt-15min}}$ and L with the parameters of the true anisotropic anomaly correlation functions. In this section $L_{\mathrm{alt-15min}}$ is used because it should be affected more by anisotropy in the anomaly correlation function than the other methods. The difference between $L_{\mathrm{alt-15min}}$ and L, L_{diff}, is defined here as

$$L_{\mathrm{diff}} = 100 \times \frac{L - L_{\mathrm{alt\_15min}}}{L}. \tag{13}$$

Comparisons between L_{diff} and the ellipse parameters of the anomaly correlations are shown in Fig. 17. Areas where L_{diff} is negative represent boxes where the altimeter overestimates the isotropic length scale. The top two panels in this figure support the idea that the impact of the altimeter sampling pattern is dependent upon the anisotropy of the anomaly correlations. These show that where the full model anomaly correlations are isotropic (i.e., the ratio of the axes is close to 1) the underestimation of the length scale by the altimeter is close to zero. As the ellipses become more anisotropic, the axis ratio increases and the amount by which the altimeter underestimates the length scale increases.

Consider now the middle panels of Fig. 17, and, in particular, the areas where L_{diff} is negative. These are mostly where the tilt of the major axis of the ellipse is around 30° or around 150°. These are approximately the angles of the *Geosat* descending and ascending ground tracks (respectively) at midlatitudes. This is to be expected: if the longest length scales of the anomaly correlation function are in the direction of the ground tracks, then these are the scales that the altimeter will be able to measure, and so the isotropic length scale, which should approximate the average of the length scales in all directions, will be overestimated.

It was seen in section 5b(3) that by calculating correlation length scales from ascending and descending

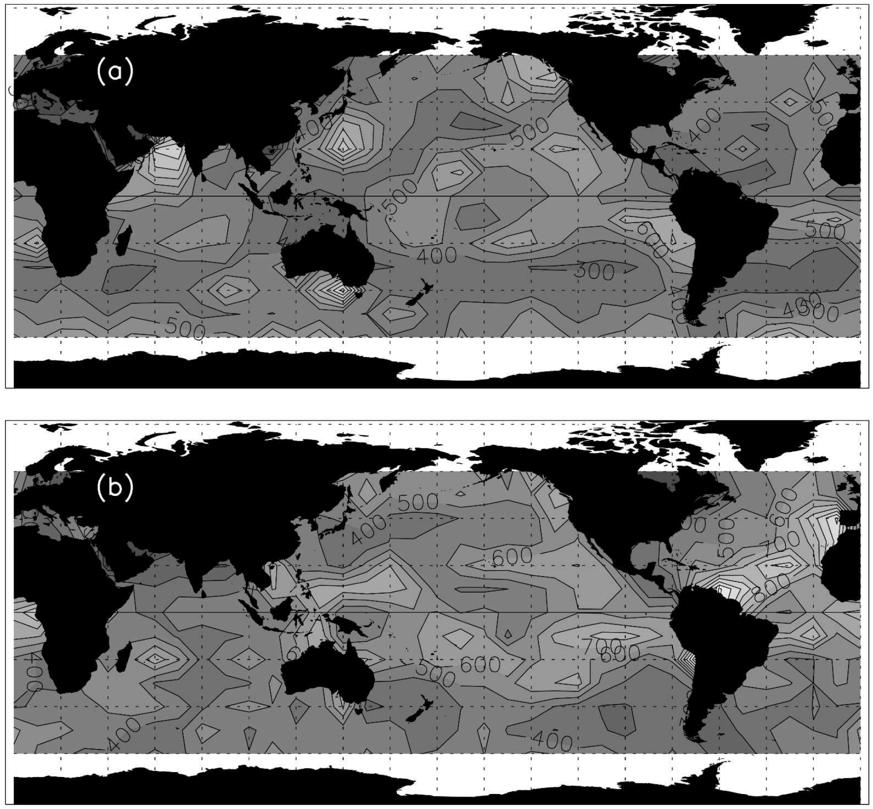

FIG. 16. Same as Fig. 10, but L_{alt} is calculated using t_{max} = 15 min.

tracks separately, it is possible to obtain some information on the anisotropy of the anomaly correlation functions. This suggests that it may be possible to use the information from ascending and descending ground tracks to provide an indication of how much the isotropic length scales should be altered to bring them closer to the true length scales. Details of this method can be found in Greenslade (2004). In summary, it was found that the difference between L_{asc} and L_{desc} does not provide enough of an indication of the anisotropy of the anomaly correlation function to be able to use this technique to adjust the isotropic length scale. This is because the ground tracks simply do not cover the range of angles needed to be able to determine how anisotropic the anomaly correlation function is. As seen in Fig. 6 there are many ellipses that are aligned directly east–west, and it is not possible for the satellite altimeter to detect this. This was also shown by the results in Fig. 14. This problem could be alleviated by the use of observations from more than one altimeter.

c. *Effect of using a constant 20° box size*

In this work, spatial correlations have been calculated over the globe within boxes of side length 20° in latitude and longitude. Because of the curvature of the earth, these boxes cover a smaller area of the ocean surface at higher latitudes than at lower latitudes. For example, the central width of a 20° box centered at the equator is approximately 2234 km, while the central width of a 20° box centered at 60°N or 60°S is only 1117 km. Thus, boxes at the equator are twice as wide as those at the highest latitudes considered here. This can be seen in Fig. 18, which shows ground tracks for the *Geosat* altimeter within a box centered at the equator and one centered at 60°S. These 20° × 20° regions are drawn with an azimuthal equidistant map projection.

The concern with a varying box size arises because if a larger box size is used, then it is possible to detect

TABLE 5. Mean and standard deviation of the differences between L and the length scales calculated from the simulated altimeter data.

	Difference (km)		Difference (% L)	
	Mean	Std dev	Mean	Std dev
2 h	70.7	137.7	10.3	21.0
15 min	84.4	148.5	12.2	22.3
ad	71.4	148.7	9.7	23.1

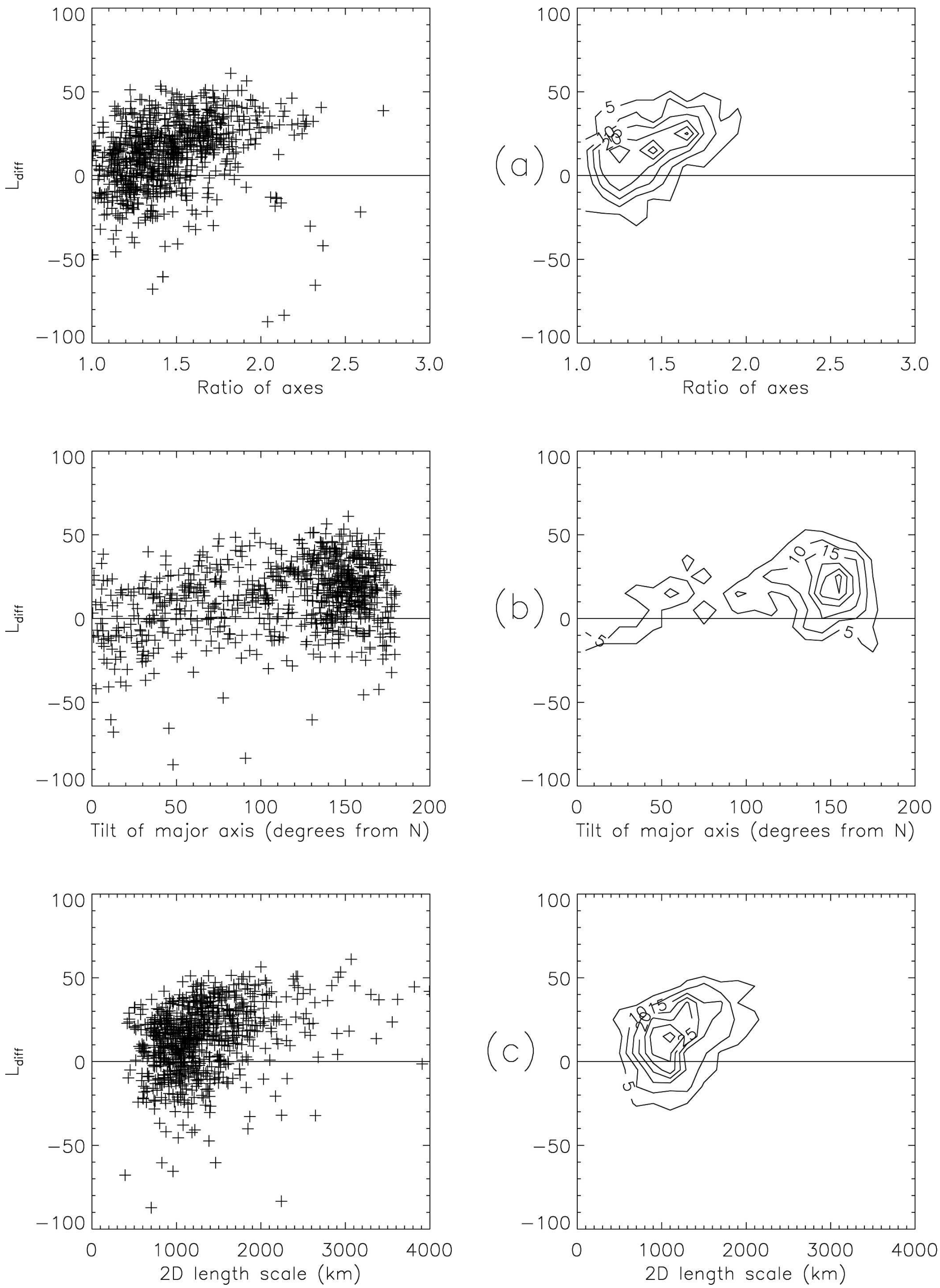

FIG. 17. L_{diff} [see Eq. (13)] as a function of the ellipse parameters of the anomaly correlation. (a) Axis ratio, (b) tilt of ellipse, and (c) length scale. In the right-hand panels, the density of the data in the left-hand panels is contoured.

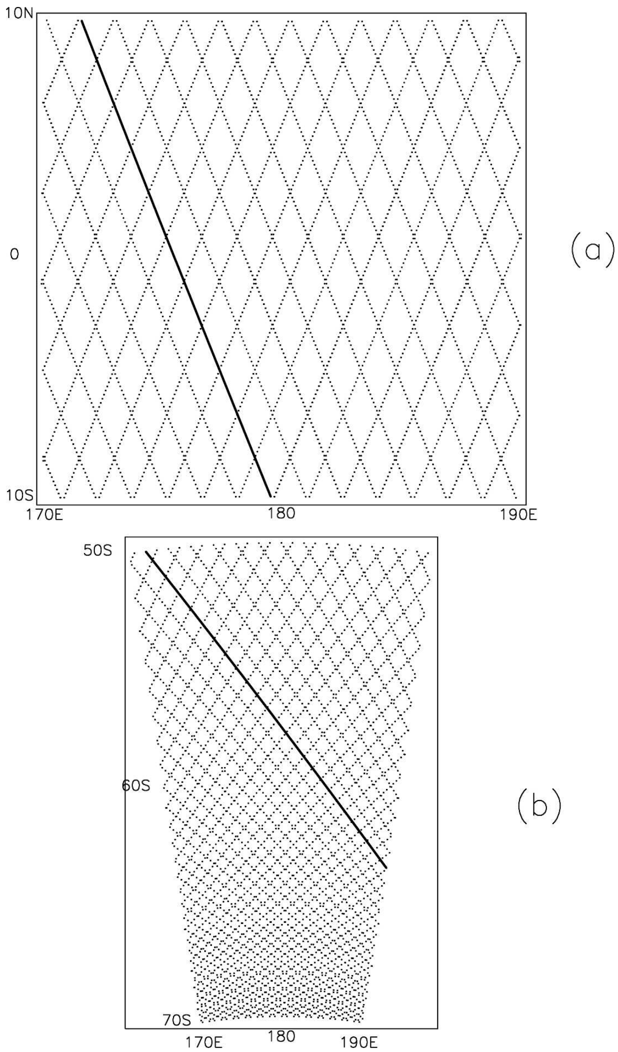

FIG. 18. *Geosat* ground tracks over a 20° box centered (a) at the equator and (b) at 60°S plotted with an azimuthal equidistant map projection.

larger signals in the SWH field, and so one might expect the correlation length scale to increase. However, the distribution of the ground tracks within a box also changes with latitude. The solid lines in Fig. 18 highlight individual ground tracks, and it can be seen that the ground tracks become more zonal at high latitudes. In fact, the ground track within the 60°S box covers a greater zonal distance than the ground track within the equatorial box. Conversely, the meridional distance covered by an individual ground track is shorter at the high latitudes.

To examine how the correlation scales might be affected by the use of different areas of the ocean surface at different latitudes, a comparison is made between correlation length scales obtained from 10° boxes and those from 20° boxes. The idea is that the difference in correlation length scales seen between a 20° box at the equator and a 10° box at the equator is comparable to the difference that might be expected to be seen between a 20° box at the equator and a 20° box at 60°S.

Figure 19 shows some examples of isotropic correlations as a function of distance for 10° and 20° boxes centered at the same location. These correlations have been calculated from the simulated altimeter data using only along-track data, that is, with $t_{\max} = 15$ min. The correlations shown in Fig. 19 are typical, and it can be seen that there is no distinct pattern to the differences between correlations from 10° boxes and those from 20° boxes. When the curve-fitting routines are applied to these functions, the behavior of the correlation function at long spatial lags has a strong influence on the resulting length scale for the 20° box. To enable a more robust comparion with the 10° boxes, the correlation functions from the 20° boxes were truncated at 1000 km before the curve-fitting routines were applied. Figure 20 shows a comparison of the length scales. The mean difference between length scales from 10° boxes and those from 20° boxes is only 3.3 km. Thus, it can be concluded that the use of a constant 20° box size over the globe is not an issue.

7. Summary

One of the main limitations to current wave data assimilation systems is the lack of an accurate representation of the structure of the background errors. The observational method of Hollingsworth and Lönnberg (1986) is one method that can be used to examine background errors. For SWH, potential long-term high-quality observations come from satellite altimeters. In this work, the impact of satellite altimeter sampling patterns on estimates of modeled SWH anomaly correlations has been examined. A set of anomaly correlations was constructed from global 0.5° spatial resolution wave model fields. The 3-month mean modeled SWH was used for the climatology. Anomaly correlations were calculated over the globe at 10° intervals, within boxes with side lengths of 20° in latitude and longitude. These correlations were fitted to analytic functions of distance and angle (anisotropic correlations), and of distance alone (isotropic correlations).

The isotropic correlation length scale L was defined to be the parameter that provided the best fit between the isotropic correlations and a SOAR function [see Eq. (10)]. It was found that L varies significantly over the globe, with typically longer scales at low latitudes and shorter scales at high latitudes. Considerable seasonal differences were found in the global distribution of L.

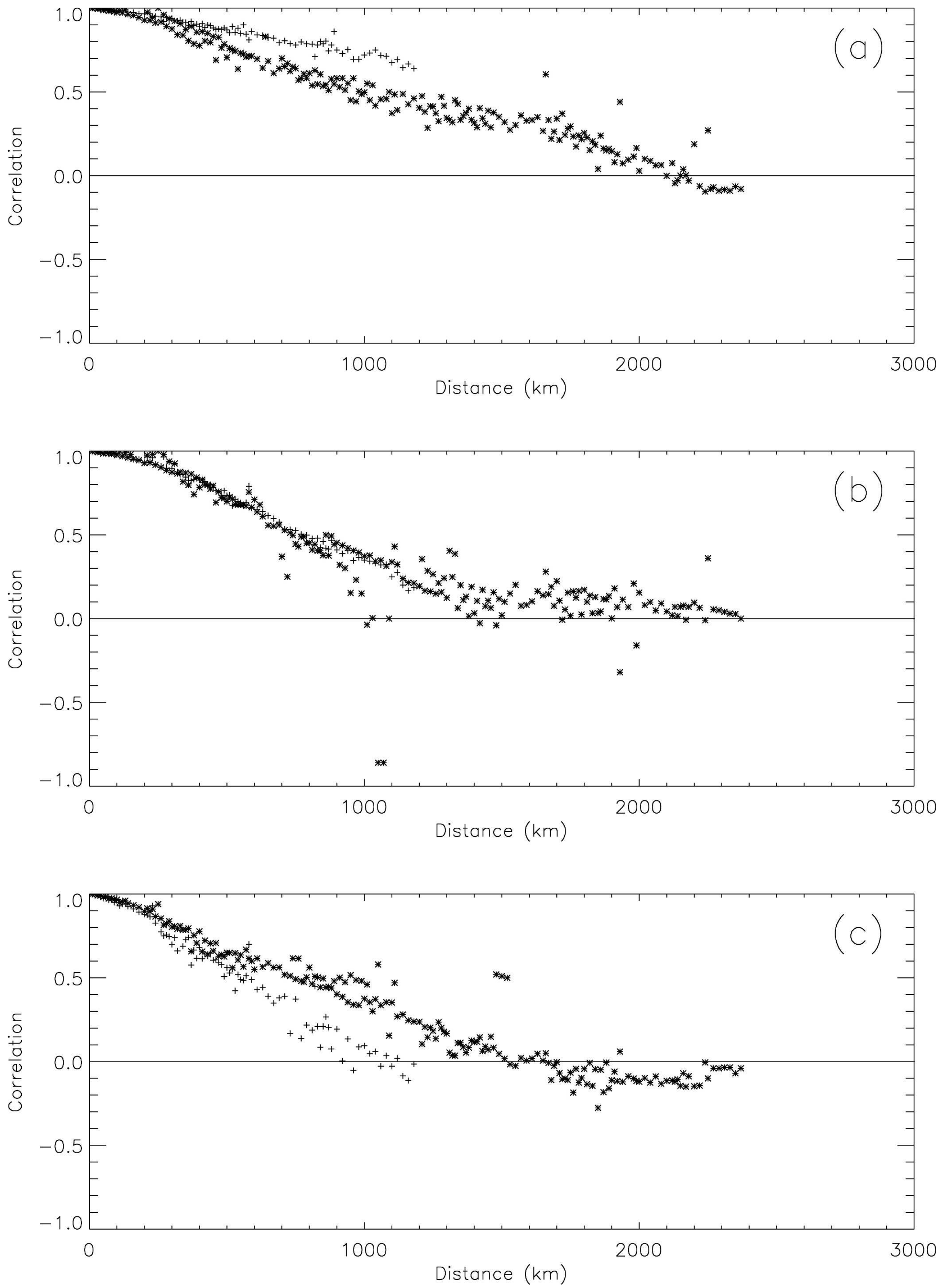

FIG. 19. Comparison between $L_{alt-15min}$ from 10° boxes (crosses) and $L_{alt-15min}$ from 20° boxes (asterisks) for boxes on the equator centered at (a) 180°, (b) 140°W, and (c) 30°W.

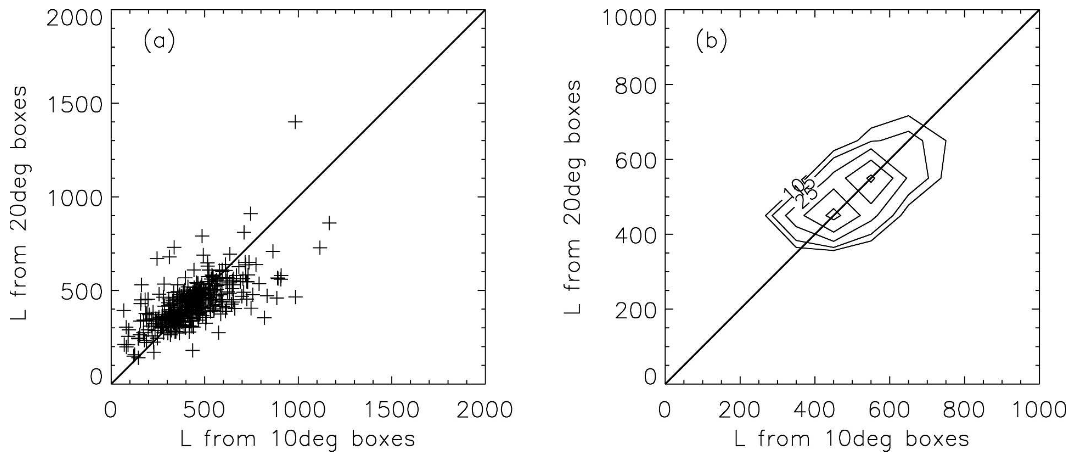

FIG. 20. (a) Comparison between $L_{\mathrm{alt-15min}}$ from 10° boxes and $L_{\mathrm{alt-15min}}$ from 20° boxes for Jul–Sep 1998. (b) Same as (a), but the number of points is contoured.

The anomaly correlation functions were found to be significantly anisotropic over most of the ocean surface. This could be because the wave systems are aligned with the prevailing winds, or it could be a result of the swell propagating and dispersing perpendicular to the direction of propagation.

Simulated satellite altimeter ground tracks were created, and the modeled SWH fields were sampled at the simulated altimeter observation locations. The anomaly correlations were recalculated from this simulated altimeter data. The simulated altimeter data were able to capture most of the geographic and seasonal variability in the isotropic correlation length scales. The best estimates of the isotropic length scales came from a method in which correlations were calculated between observations that were within 2 h of each other. This method was found to underestimate the isotropic anomaly correlation length scale by approximately 10%.

The simulated observations were not so successful in producing realistic anisotropic correlation functions. This is because of the lack of information in the zonal direction in the simulated altimeter data. However, examination of correlations along ascending and descending ground tracks separately provided some indication of the areas on the globe for which the anomaly correlations are more anisotropic than others.

This work has demonstrated that satellite altimeter data are able to reproduce the observed variability (both spatial and temporal) in model anomaly correlations. The next step is to apply these results to real altimeter observations. This is done in Greenslade and Young (2004), where the *European Remote Sensing Satellite* (*ERS*)*-2* altimeter data are compared to wave model output directly and a new background error correlation matrix for use in wave data assimilation systems is presented.

Acknowledgments. The authors thank Christian Jakob, Hendrik Tolman, Robert Jensen, and the anonymous reviewers for comments on the manuscript. Financial assistance in the form of a Ph.D. scholarship for D. J. M. Greenslade was provided by the Australian Bureau of Meteorology.

REFERENCES

Bender, L. C., 1996: Modification of the physics and numerics in a third-generation ocean wave model. *J. Atmos. Oceanic Technol.,* **13,** 726–750.

Bidlot, J. R., P. A. E. M. Janssen, B. Hansen, and H. Günther, 1997: A modified set up of the advection scheme in the ECMWF wave model. ECMWF Tech. Memo. 237, 31 pp.

Breivik, L. A., and M. Reistad, 1994: Assimilation of ERS-1 altimeter wave heights in an operational numerical wave model. *Wea. Forecasting,* **9,** 440–451.

Daley, R., 1991: *Atmospheric Data Analysis.* Cambridge University Press, 457 pp.

Garratt, J. R., 1992: *The Atmospheric Boundary Layer.* Cambridge University Press, 316 pp.

Greenslade, D. J. M., 2001: The assimilation of ERS-2 significant wave height data in the Australian region. *J. Mar. Syst.,* **28,** 141–160.

——, 2004: The structure of the background errors in a global wave model. Ph.D. thesis, University of Adelaide, 194 pp.

——, and I. R. Young, 2004: Background errors in a global wave model determined from altimeter data. *J. Geophys. Res.,* **109,** C09007, doi:10.1029/2004JC002324.

Günther, H., W. Rosenthal, and M. Dunckel, 1981: The response of surface gravity waves to changing wind directions. *J. Phys. Oceanogr.,* **11,** 718–728.

Hollingsworth, A., and P. Lönnberg, 1986: The statistical structure of short-range forecast errors as determined from radiosonde data. Part I: The wind field. *Tellus,* **38A,** 111–136.

Julian, P., and H. J. Thiebaux, 1975: On some properties of cor-

relation functions used in optimum interpolation schemes. *Mon. Wea. Rev.,* **103,** 605–616.
Komen, G. J., L. Cavaleri, M. Donelan, K. Hasselmann, S. Hasselmann, and P. A. E. M. Janssen, 1994. *Dynamics and Modelling of Ocean Waves.* Cambridge University Press, 532 pp.
Lionello, P., H. Günther, and P. A. E. M. Janssen, 1992: Assimilation of altimeter data in a global third-generation wave model. *J. Geophys. Res.,* **97,** 14 453–14 474.
Lorenc, A. C., 1981: A global three-dimensional multivariate statistical interpolation scheme. *Mon. Wea. Rev.,* **109,** 701–721.
Mastenbroek, C., V. K. Makin, A. C. Voorrips, and G. J. Komen, 1994: Validation of ERS-1 altimeter wave height measurements and assimilation in a North Sea wave model. *Global Atmos. Ocean Syst.,* **2,** 143–161.
National Meteorological Operations Centre, 1998: Upgrade of the Global Analysis and Prediction (GASP) system. *Operations Bulletin,* No. 45, Bureau of Meteorology, Australia, 36 pp.
——, 1999: Changes to the operational sea state forecast system. *Operations Bulletin,* No. 47, Bureau of Meteorology, Australia, 7 pp.
Piexoto, J. P., and A. H. Oort, 1992: *Physics of Climate.* American Institute of Physics, 520 pp.
Seaman, R. S., 1982: A systematic description of the spatial variability of geopotential and temperature in the Australian region. *Aust. Meteor. Mag.,* **30,** 133–141.
——, and F. J. Gauntlett, 1980: Directional dependence of zonal and meridional wind correlation coefficients. *Aust. Meteor. Mag.,* **28,** 217–221.
Seaman, R., W. Bourke, P. Steinle, T. Hart, G. Embery, M. Naughton, and L. Rikus, 1995: Evolution of the Bureau of Meteorology's Global Assimilation and Prediction System. Part 1: Analyses and initialization. *Aust. Meteor. Mag.,* **44,** 1–18.
Snyder, R. L., F. W. Dobson, J. A. Elliot, and R. B. Long, 1981: Array measurements of atmospheric pressure fluctuations above surface gravity waves. *J. Fluid Mech.,* **102,** 1–59.
Voorrips, A. C., K. Makin, and S. Hasselmann, 1997: Assimilation of wave spectra from pitch-and-roll buoys in a North Sea wave model. *J. Geophys. Res.,* **102,** 5829–5849.
The WAMDI Group, 1988: The WAM model—A third generation wave prediction model. *J. Phys. Oceanogr.,* **18,** 1775–1810.
Young, I. R., 1999: *Wind Generated Ocean Waves.* Elsevier Science, 288 pp.
——, and T. J. Glowacki, 1996: Assimilation of altimeter wave height data into a spectral wave model using statistical interpolation. *Ocean Eng.,* **23,** 667–689.